Indian Journal of Chemistry
Vol. 56A, May 2017, pp. 479-487

Structural characterization and photocatalytic properties of hydrothermally synthesized Ni^{2+}-TiO_2 nanoparticles for dye degradation under direct sunlight

Ravi Kamble[a], Sandip Sabale[b,] *, Prashant Chikode[a], Vijaya Puri[c] & Smita Mahajan[a]

[a]Department of Physics, Jaysingpur College, Jaysingpur 416 101, India
Email: dr_smitamahajan@yahoo.com (SM)

[b]PG Department of Chemistry, Jaysingpur College, Jaysingpur 416 101, India
Email: srsabale@gmail.com (SB)

[c]Department of Physics, Shivaji University, Kolhapur 416 004, India

Received 13 November 2016; revised and accepted 28 April 2017

A Ni^{2+}-TiO_2 photocatalyst, efficient and highly active in sunlight has been prepared by a simple hydrothermal method using titanium isopropoxide (TTIP) precursor. The synthesized nanoparticles (NPs) have been analysed to determine its structural, optical, morphological and compositional properties using X-ray diffraction, Raman, UV-DRS, photoluminescence, XPS, TEM and EDS. The EDS micrograph confirms the existence of Ni^{2+} atoms (0.65, 1.32 and 1.60 wt.%) in the TiO_2 matrix. The average particle size obtained from TEM is 8-11 nm and is in good agreement with XRD results. Raman bands at 641.44 cm^{-1}, 517.42 cm^{-1} and 398.43 cm^{-1} further confirm pure phase anatase in all samples. XPS shows the substitution of Ti^{4+} ions by Ni^{2+} ions in the TiO_2 host lattice. The photocatalytic activity of these nanoparticles have been studied using malachite green dye under UV light, visible light and direct sunlight. The crystallite size and band gap decreases with increase in Ni^{2+} concentration which increase its catalytic activity under sunlight. The photocatalyst, Ni^{2+}-TiO_2 (1.60 wt.%), shows excellent photocatalytic activity in the visible and direct sunlight and hence it is a promising for environmental friendly photocatalytic applications.

Keywords: Photocatalytic activity, Nanoparticles, Hydrothermal synthesis, Dye degradation, Degradation, Nickel, Titania, Malachite green

Over the past few decades, rampant use of pesticide, industrial chemicals and different types of dyes in cosmetic, paper, leather and textile industries has led to severe pollution of water. Textile waste water, is a well known cause of water pollutant and has high levels of organic-inorganic salt with intense colors. These pollutants have low degradability, are highly toxic and pose a significant threat to the surrounding ecosystem and human health. The degradation process of dyes which is slow under solar irradiation has thus become an important environmental issue.

Photocatalysis, an advanced oxidation process (AOPs), has received much attention in recent years for enhancing the degradation of pollutants such as textile dyes[1-4]. Photocatalysis involves the excitation of semiconductor under sunlight, UV light and visible light. Here electrons (e^-) are excited to conduction band, leaving holes (h^+) in the valence band[5, 6]. These electrons reduce the molecular oxygen adsorbed on the surface to form superoxide ion-radical. Further reaction leads to the formation of peroxides or ·OH radicals. The pollutants are degraded directly by photogenerated holes or by the hydroxyl ion[7-9].

Titania (TiO_2) has been extensively studied as a photocatalyst and has gained much attention as it is chemically and thermally stable, non-toxic, cheap and biologically inert. Titania has been widely used in dye sensitized solar cells, paints, sensors, Li-ion batteries, etc., and also extensively used for its photocatalytic activity. For industrial applications, anatase TiO_2 has been preferred over rutile and brookite due to its higher photocatalytic activity[10, 11].

TiO_2 has a band gap of 3.2 eV and limit its photocatalytic activity to UV irradiation (λ< 380 nm, 5% of the solar spectrum). The photocatalytic activity of TiO_2 can be improved by shifting its optical response in the visible wavelength, this can be achieved by doping TiO_2 with transition metals[12, 13] like Fe^{3+} (ref. 14) , Mn^{2+} (ref. 15), Cu^{2+} (ref. 16), Ni^{2+} (ref. 17), Co^{2+} (ref. 18) and $V^{4+/5+}$ (ref. 19). Among these metals, Ni^{2+} has been extensively studied as it is observed that Ni^{2+} suppresses electron(e^-)-hole(h^+) recombination which improves the photocatalytic process.

Herein, Ni^{2+}-TiO_2 NPs with concentration 0.65, 1.32 and 1.60 wt.% were hydrothermally synthesized using titanium isopropoxide (TTIP) precursor. The obtained samples were characterized using XRD, UV, Raman, PL, XPS, TEM and EDS data. The efficiency of photocatalytic activity of prepared samples was studied using malachite green dye in UV light, visible light and direct sunlight.

Materials and Methods

All chemicals used were of analytical grade and were used as received without further purification. Titanium(IV) tetraisopropoxide (TTIP, 98%) and nickel nitrate hexahydrate (99%) were purchased from Spectrochem. Pvt. Ltd., Mumbai (India) and SD Fine-Chem Ltd., Mumbai (India) respectively. Glacial acetic acid (99%) was purchased from the Pune Chemical Laboratory., Pune (India), absolute ethanol (99.9%) and doubly distilled water were used throughout the experiment.

Synthesis of Ni^{2+}-TiO_2 nanoparticles

Pure TiO_2 and Ni^{2+}-TiO_2 NPs were synthesized by hydrothermal method in a stainless steel autoclave. In the preparation, 5 mL glacial acetic acid was mixed with 5 mL TTIP with constant stirring to get a clear solution. The stirring was continuous for 15 min followed by the addition of 10 mL water. To achieve the desired concentration of Ni^{2+} ion as a dopant (~1-3 wt.%) in the TiO_2 host lattice, calculated amount of nickel nitrate was dissolved in 10 mL water. This dopant solution was added to the mixture and stirred vigorously to obtain a clear solution. The obtained solution was transferred to a teflon lined stainless steel autoclave which was sealed and heated at 120 °C for 5 h. After heating, the autoclave was allowed to cool down in a muffle furnace. The final product was washed with 30 mL ethanol. The supernatant liquid was discarded and the residue obtained was dried at 60 °C to get TiO_2 NPs. The obtained samples were annealed at 350 °C for 2 h. All the samples of pure TiO_2 and (1-3 wt.%) Ni^{2+}-TiO_2 were prepared by this method.

Photocatalytic activity of Ni^{2+}-TiO_2 nanoparticles

The photocatalytic activity of the obtained samples were evaluated for the degradation of malachite green (50 ppm) under UV light, visible light and sunlight. A photoreactor was kept open in air to get sufficient oxygen for the photooxidation reaction. In this experiment 5.0 mg photocatalyst was added to the photoreactor containing 50 mL (50 ppm) of dye solution. Before irradiation, the solution was stirred for 30 min to ensure adsorption-desorption equilibrium and then it is exposed to UV light. At particular time intervals, aliquots were collected from the photoreactor. The NPs were separated out by centrifugation and the solution was further used to monitor the concentration of malachite green by recording the absorbance of the solution on a UV-visible double beam spectrophotometer (Lab India, model-UV-3000^+). Similar experiments were performed for the degradation of malachite green dye in visible light and direct sunlight under the same reaction conditions.

Characterization

The phase purity and crystallinity of samples were identified using a Rigaku miniflex 600 X-ray diffractometer (XRD) with Cu Kα radiation ($\lambda = 1.54056$) at a scanning rate of 2° (2θ) min^{-1} in the 2θ range from 20-80°, operated at 40 kV and 40 mA. The diffused reflectance spectra (DRS) were recorded in the range of 200-600 nm on a UV-visible NIR spectrophotometer (Jasco, model V-770). The shape and size of the NPs were investigated using a Jeol 3010 TEM instrument. Elemental composition was determined from energy dispersive X-ray spectrometeric (EDS) analysis (model Jeol JSM 5600). The photoluminescence (PL) spectra of the samples were recorded on Jasco spectrofluorometer (model FP 8200). X-ray photoelectron spectroscopy (Surface Nano Analysis GmbH, SPECS, Germany) was used for determining the surface compositions of the photocatalysts. These data have been recorded using Al-Kα (1486.61 eV) X-rays. Raman spectra were recorded using a micro-Raman spectrometer (Horiba Jobin Vyon, France) equipped with a 488 nm excitation laser, an edge filter for Rayleigh line rejection, an 1800 g/mm grating and a CCD detector. The laser was focused on the sample in a dimension of ~1 micron using a 50X objective lens with the overall spectral resolution of the system as ~1 cm^{-1}.

Results and Discussion

X-ray diffraction patterns of pure TiO_2 and Ni^{2+}-TiO_2 samples are shown in Fig. 1(A). The diffraction peaks at $2\theta = 25.50°$, 37.92°, 48.00°, 53.71°, 54.88°, 62.72°, 68.88°, 70.33° and 75.12° corresponds to (101), (004), (200), (105), (211), (204), (116), (220) and (215) plane respectively, shows the formation of pure phase anatase TiO_2 (JCPDS 21-1272). The major

peak (101) of Ni^{2+}-TiO_2 was found to be shifted to a lower angle from 25.50° to 25.29° (Fig. 1B), due to doping of Ni^{2+}-TiO_2, which confirms that only one crystalline phase was formed during the synthesis process. No extra peak corresponding to rutile phase or oxide of the dopant metal ions was found. The crystallite size was calculated using Scherer's equation[20], $D = 0.9\ \lambda/\beta \cos\theta$; where '$D$' is the crystallite size, 'λ' is the wavelength of the X-ray radiation (Cu-Kα = 0.15418 nm), 'θ' is the diffraction angle of the strongest characteristic peak and 'β' is the full width at half maximum (FWHM). The X-ray density was calculated for the samples by using formula, $\rho = nM / NV$; where 'M' is the molecular weight, 'N' is Avogadro's number and 'V' is the volume of unit cell. For anatase phase n is four and for rutile phase n is two. Further, the surface area (S_a) was calculated using formula[21], $S_a = 6/D\times\rho$, where 'D' is crystallite size and 'ρ' is density. The densities of all the Ni^{2+} doped samples are close to each other, but higher than that of pure TiO_2. The calculated crystallite sizes, lattice parameters, density and surface area are given in Table 1. It is seen that with increasing dopant concentration, the crystallite size decreases. The decrease in crystallite size can be correlated to the increase in structural defects that prevent particle growth. The ionic radius of Ni^{2+} ion (0.72 Å) is similar to that of Ti^{4+} ion (0.68 Å), due to which it is is possible to replace Ti^{4+} ions by Ni^{2+} ions in TiO_2 lattice[22, 23, 17]. Doping of Ni^{2+} generates oxygen vacancies in the lattice of TiO_2 to maintain the charge neutrality.

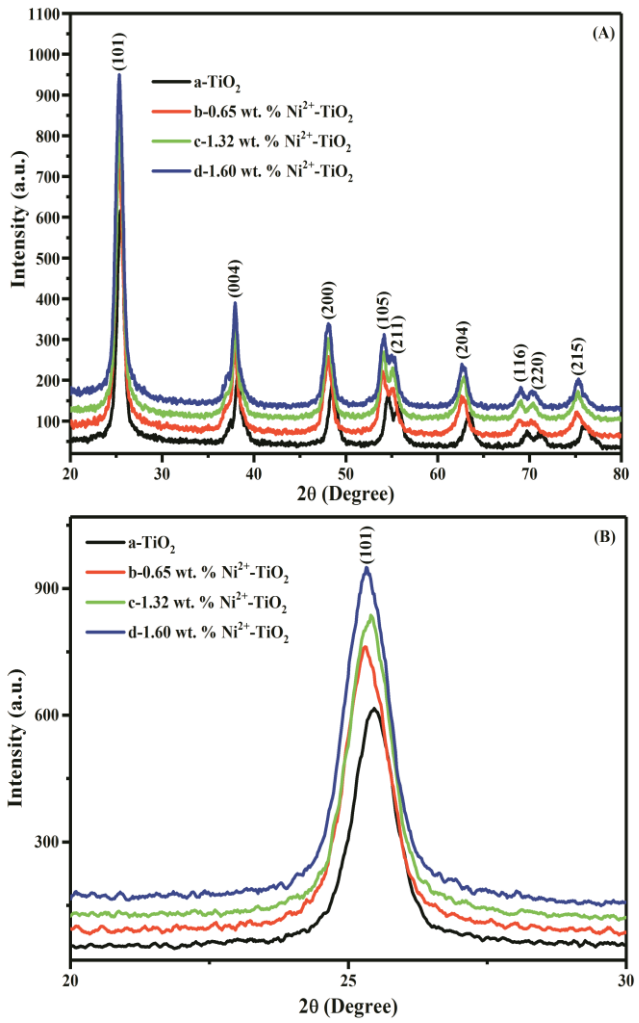

Fig. 1 - (A) XRD patterns and (B) shift in 2θ angle of (a) pure TiO_2, (b) 0.65 wt.%, (c) 1.32 wt.% and (d) 1.60 wt.% Ni^{2+}-TiO_2 NPs.

UV-visible diffuse reflectance spectra of pure TiO_2 and Ni^{2+}-TiO_2 NPs annealed at 350 °C are shown in Fig. 2. The UV-visible absorption spectra were recorded at room temperature in the range of 200-600 nm. The spectrum for the TiO_2 NPs shows a sharp absorption edge at 390 nm, while the absorption spectra of Ni^{2+}-TiO_2 is shifted to the visible region of the spectrum. The band gap energy of all the obtained samples was determined using formula, $(\alpha h\vartheta)^n = B(h\vartheta - E_g)$, where '$h\vartheta$' is the photon energy, 'α' is the absorption of the nanocrystalline TiO_2 powder, 'B' is a constant relative to the material, E_g is the separation between bottom of the conduction band and top of the valence band and n is a constant. The 'n' value depends on the nature of

Table 1 – Crystallite size (D_{XRD}), diameter (D_{TEM}), lattice constant (*a/b*, *c*), unit cell volume (*V*), X-ray density (ρ), surface area (S_a), band gap and EDS composition of the catalyst samples

Sample	D_{XRD} (nm)	D_{TEM} (nm)	Lattice constant (Å)		*V* (Å)	ρ (g/cm^3)	S_a (m^2/g)	Band gap (eV)	Comp. (wt.%)		
			a/b	*c*					Ti	O	Ni
Pure TiO_2	11.0	11.0	3.7754	9.5099	135.55	2.12	257.0	3.18	56.34	43.66	0.0
0.65 wt% Ni^{2+}-TiO_2	9.56	10.0	3.7804	9.5011	135.78	3.67	171.01	2.56	58.08	41.27	0.65
1.32wt% Ni^{2+}-TiO_2	8.46	9.0	3.7796	9.5001	135.71	3.68	192.04	2.52	54.46	44.22	1.32
1.60 wt% Ni^{2+}-TiO_2	7.86	8.0	3.7836	9.4977	135.96	3.66	208.56	2.43	54.85	43.55	1.60

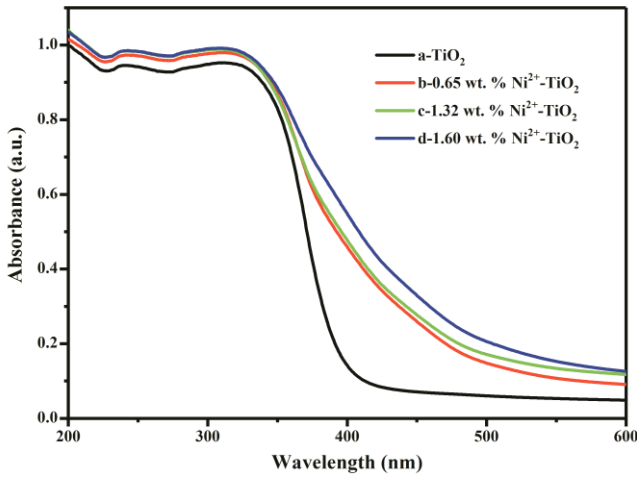

Fig. 2 – UV-visible diffuse reflectance spectra of (a) pure TiO_2, (b) 0.65 wt.%, (c)1.32 wt.% and (d) 1.60 wt.% Ni^{2+}-TiO_2 NPs.

transition. For example n is equal to 2 for direct band gap, 2/3 for direct forbidden gap and 1/2 for indirect band gap[24]. The calculated band gap energy values are given in Table 1 which show that the band gap energy decreases as Ni^{2+} content increases from 0.65 wt.% to 1.60 wt.%. The absorption spectra (Fig. 2) of the doped samples show a stronger visible light absorption indicating the decrease in band gap with doping due to the formation of new energy level for Ni^{2+}/Ni^{+} below the conduction band and above the valence band edge of TiO_2[25]. The bathochromic shift in the band gap transition takes place as new energy levels and oxygen vacancies are generated by metal doping. Further, there is charge transfer between a dopant and conduction or valence band or a *d-d* transition in the crystal field according to the energy level due to visible light absorption[26]. The changes in the color of the samples observed specifically, white for TiO_2 and pale yellow for Ni^{2+}-TiO_2, which can be associated with the increase in the visible light absorption region.

The shape and size of obtained particles were characterized by TEM. TEM micrographs and SAED pattern of pure TiO_2 are as shown in Fig. 3A (a) and (b) while that of Ni^{2+}-TiO_2 (1.60 wt.%) NPs are as shown in Fig. 3(c) and (d) respectively. It is evident from the TEM micrographs that the synthesized Ni^{2+}-TiO_2 NPs have agglomerated, uneven and non-spherical morphology. The particle size obtained from a TEM micrograph is within the range 8-11 nm, which is in good agreement with the XRD analysis. Fig. 3B (e) and (f) shows the EDS spectrum of as synthesized pure TiO_2 and Ni^{2+}-TiO_2 (1.60 wt.%) NPs. which indicates that Ni^{2+} ions have been successfully integrated into TiO_2 matrix, in a weight percent very close to that mentioned for synthesis of TiO_2 and Ni^{2+}-TiO_2 NPs.

The room temperature Raman spectra were recorded for pure TiO_2 and (0.65-1.60 wt.%) Ni^{2+}-TiO_2 NPs to investigate the structural distortion of the crystal lattice after doping (Fig. 4). Phase pure anatase TiO_2 with two formula units per primitive cell has six Raman active modes and three infrared (IR) active modes as found from the factor group analysis. The main peak E_g appears at 144 cm^{-1} which is followed by two intense E_g peaks at 200 and 641.44 cm^{-1} respectively. Other excepted active modes B_{1g} = 398.43 cm^{-1}, A_{1g} = 517.42 cm^{-1}, corresponding to the Raman active modes are present in the spectra of all samples, which indicates that anatase TiO_2 NPs are the principal species[27]. Compared to pure TiO_2, the Raman E_g peak of doped TiO_2 NPs with 0.65-1.60 wt.% of Ni^{2+} is shifted to 149 cm^{-1} and exhibits a decrease in peak intensity as well as changes in FWHM. The shift in the E_g peak (144 cm^{-1}) frequency and decrease in the intensity has been reported in previous reports[28]. The Raman spectra for Ni^{2+}-TiO_2 NPs indicate that the peaks of all doped samples shift towards the lower wave number and there is no indication of the presence of rutile or any secondary phases. The phonon confinement model has been used for the changes using the Heisenberg uncertainty principle, $\Delta X\ \Delta P = h/2$, where ΔX, ΔP and h are the particle size, phonon momentum distribution and 'h' is Plancks constant. As the particle size ΔX decreases, the phonon momentum distribution ΔP increases and thus the spectrum gets contribution from phonons away from the zone center. This result shows asymmetric broadening of the Raman active peak. In many of the doped TiO_2 system; the shifting is attributed to a reduction in cell size after doping[29].

The valence state, substitution and contents of Ni^{2+}-TiO_2 NPs were examined by XPS analysis (Fig. 5a). In the survey scan spectrum, a peak was observed at 284.22 eV, indicating carbon impurities arising from the background of XPS analysis. The XPS survey scans spectrum of the 1.60 wt.% Ni^{2+}-TiO_2 sample shows the existence of Ni, O and Ti ions in an almost stoichiometric composition. Figure 5b shows the core level Ti 2*p* spectra of Ni^{2+}-TiO_2 sample. For anatase TiO_2, Ti $2p_{3/2}$ and Ti $2p_{1/2}$, peaks are observed at 459.41 and 465.21 eV respectively. The splitting between the Ti $2p_{3/2}$ and Ti $2p_{1/2}$ is 5.8 eV,

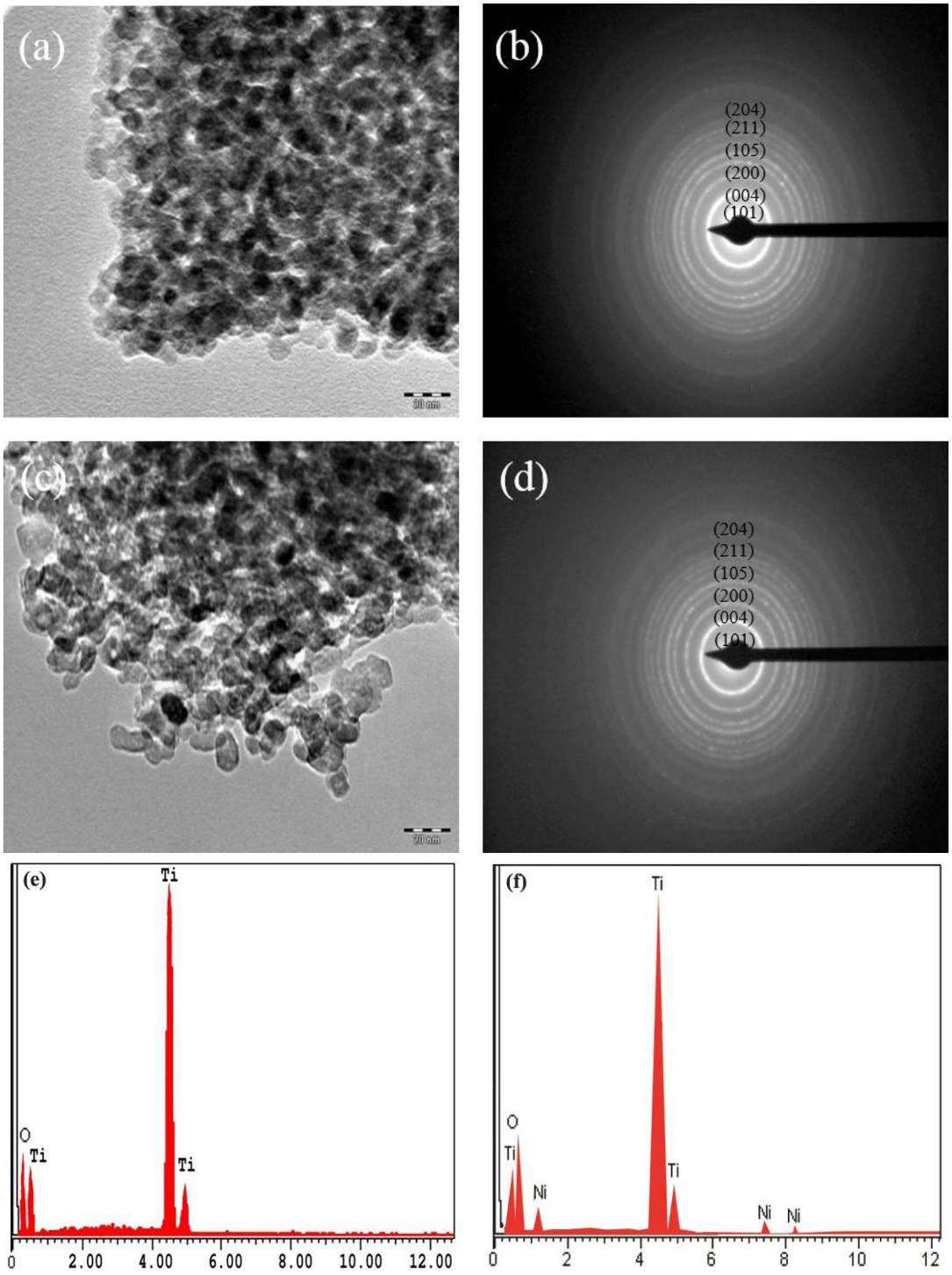

Fig. 3 – (a & c) TEM images (b & d) SAED patterns and (e & f) EDX patterns of pure TiO_2 and 1.60 wt.% Ni^{2+}-TiO_2 NPs respectively.

which is the normal state of Ti^{4+} ion in the sample[30]. The XPS spectra of O1*s* configuration is shown in Fig. 5c. The binding energies at 530.64 eV and 529.83 eV reveals the existence of surface hydroxyl groups. The O1*s* peak indicates binding energy arises from titanium lattice[19]. In the Ni 2*p* spectrum of the 1.60 wt.% Ni^{2+}-TiO_2, the peaks at 851.76 eV and 871.13 eV correspond to Ni $2p_{3/2}$ and Ni $2p_{1/2}$

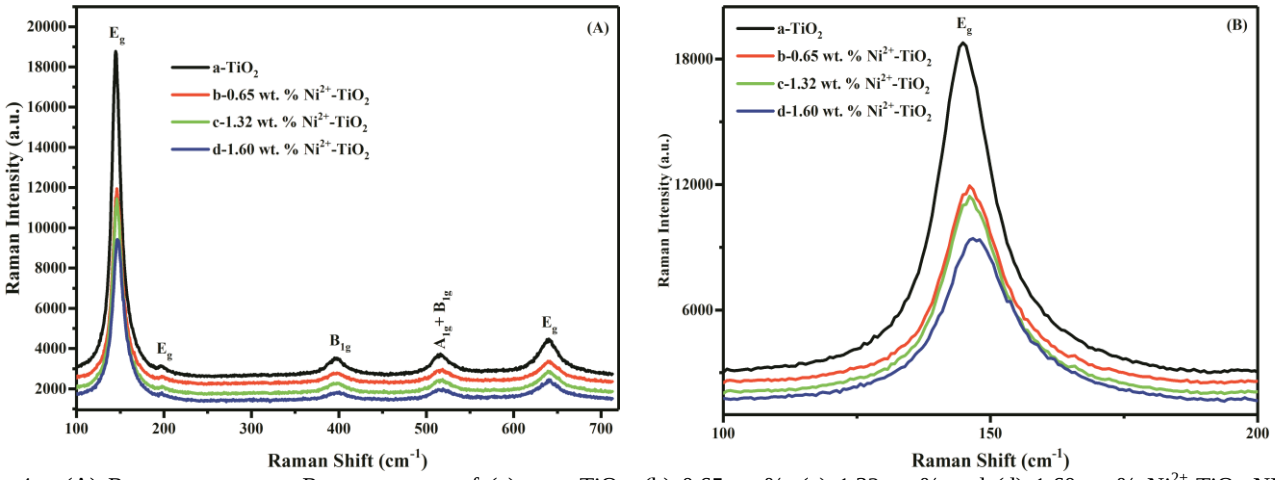

Fig. 4 – (A) Room temperature Raman spectra of (a) pure TiO_2, (b) 0.65 wt.%, (c) 1.32 wt.% and (d) 1.60 wt.% Ni^{2+}-TiO_2 NPs. (B) Shifting of peak to higher wave number with increasing dopant concentration and changes in position and FWHM with increasing Ni^{2+} concentration.

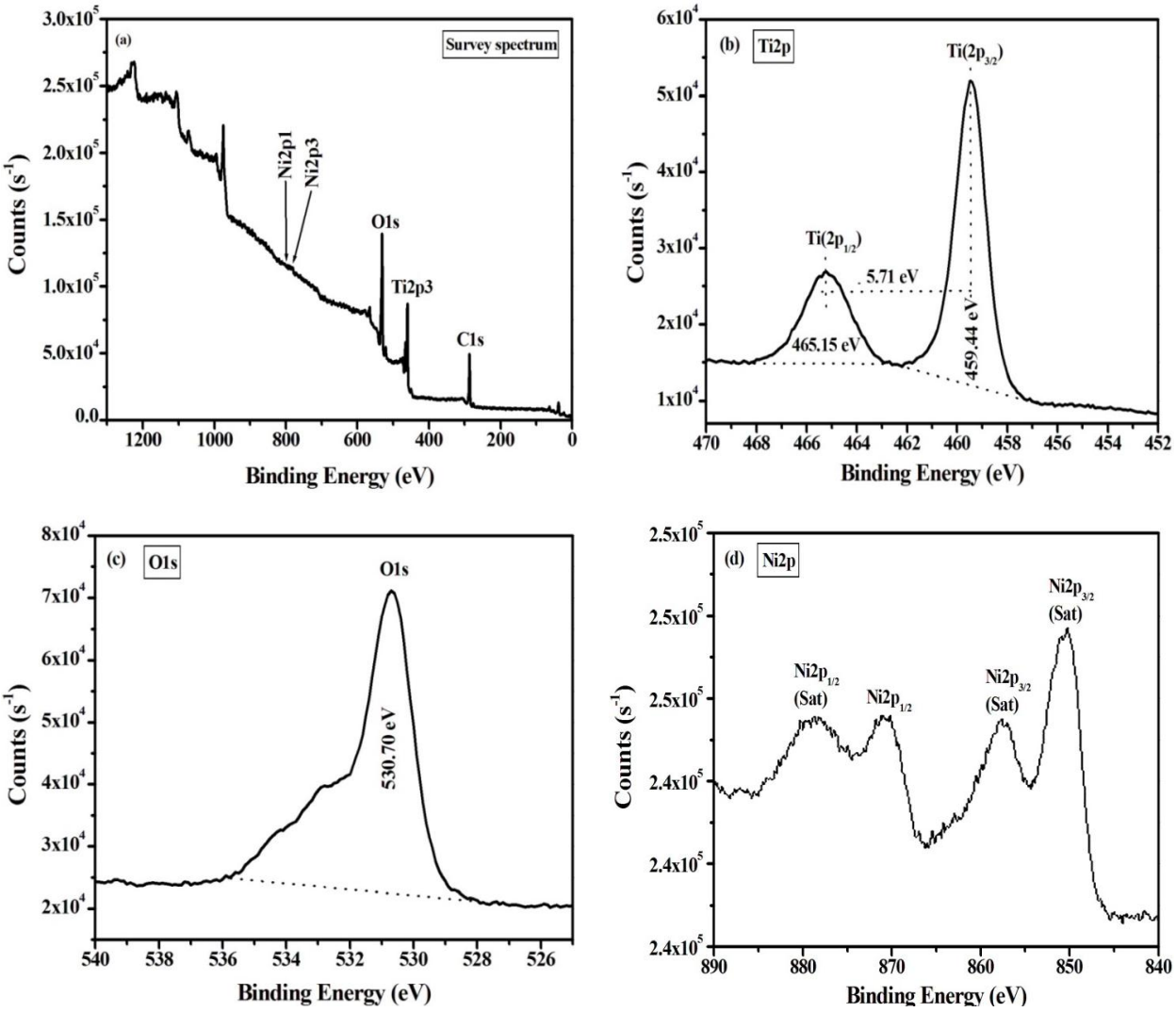

Fig. 5 – XPS for 1.60 wt.% Ni^{2+}-TiO_2 sample. [(a) survey spectrum; (b) Ti 2*p*; (c) Ni 2*p*; (d) O 1*s*].

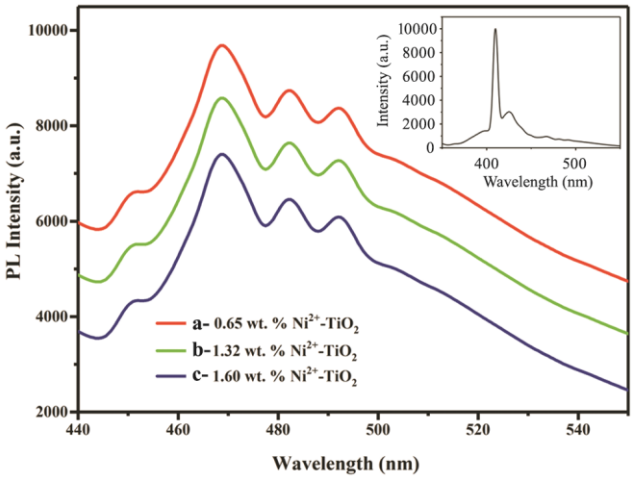

Fig. 6 – PL spectra of Ni^{2+}-TiO_2 NPs for (a) 0.65 (b) 1.32 and (c) 1.60 wt.%. [Inset showing the the PL spectrum of pure TiO_2 NPs].

respectively (Fig. 5d). The binding energy difference between Ni $2p_{3/2}$ and Ni $2p_{1/2}$ core level is 19.37 eV, which is a different from the value of metallic Ni (17.27 eV) and NiO (17.49 eV)[26]. The satellite peaks at 858.78 eV and 878.61 eV can also be observed, which are due to the multi-electron excitation[31]. XPS results correlate with the EDS results, confirming that Ni^{2+} ions are doped up to 1.60 wt.% into the TiO_2 host lattice.

Fluorescence emission spectrum (PL) is an useful method to study the electronic structure and optical properties of semiconductor materials. PL emission spectra can be used to analyse the fate of photo-generated electrons and holes in a semiconductor, since photoluminescence emission results from the recombination of free charge carriers. The PL emission spectra of pure TiO_2 and Ni^{2+}-TiO_2 NPs were recorded at an excitation wavelength of 330 nm and the emission peak of pure TiO_2 was observed at wavelength 411.13 nm. The increase in Ni^{2+} concentration shifts the wavelength towards the higher region (469, 483 and 497 nm) with decreasing peak intensity (Fig. 6). The recombination rate of photogenerated charge carriers are reduced by surface defects. The oxygen vacancies and metal ions trap the excited electrons and holes respectively. The excited electrons can migrate from the valence band to the new energy levels introduced by doping Ni^{2+} and causes decrease in the PL intensity[32].

Photocatalytic activity

In order to evaluate the photocatalytic activity, the degradation of malachite green dye as a model under UV, visible and sunlight irradiation in presence of Ni^{2+}-TiO_2 NPs suspension was investigated (Fig. 7). The absorption of the dye solution was measured

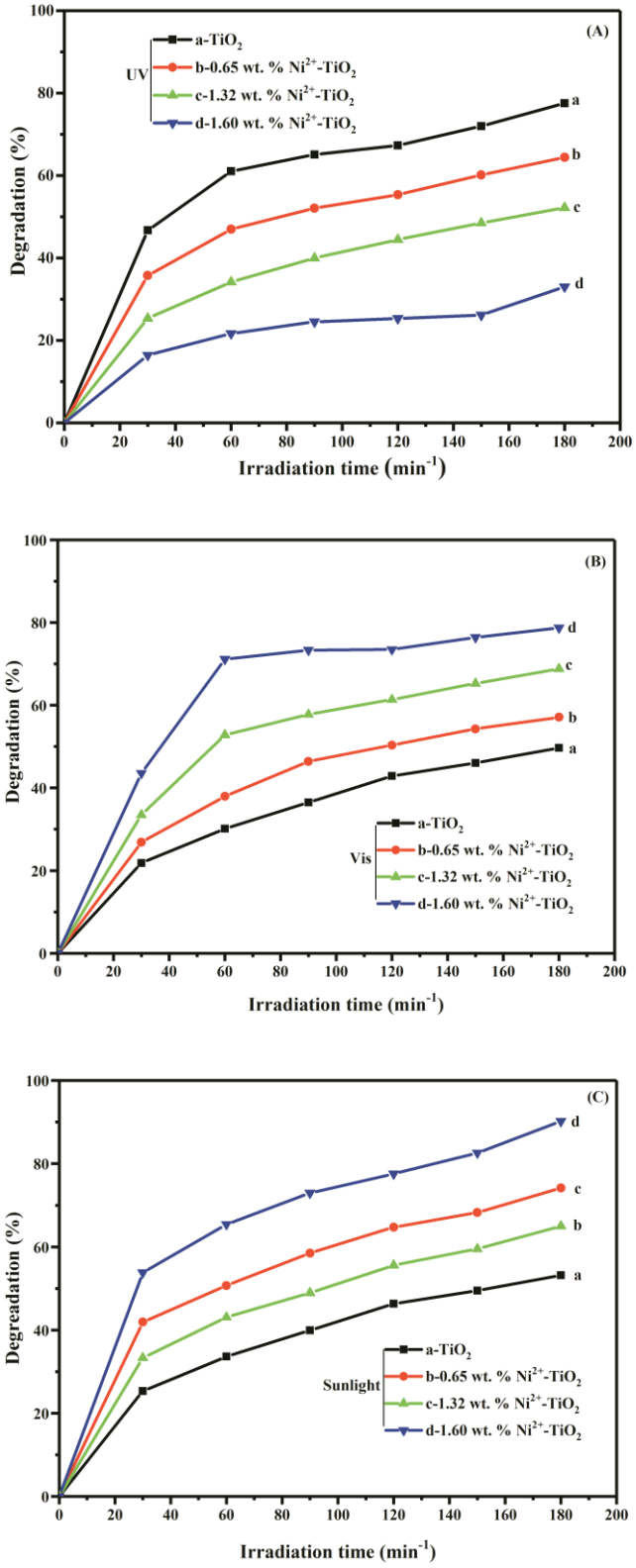

Fig. 7 – Photocatalytic activity of pure TiO_2, and 0.65, 1.32 and 1.60 wt.% Ni^{2+}-TiO_2 samples under (A) UV light (B) visible light and (C) direct sunlight for malachite green dye.

using UV-visible spectrophotometer at its characteristic wavelength. The percentage degradation of each dye at different irradiated time intervals was calculated according to the equation[33], Percentage degradation = $[1-(A_t/A_o)]\times100$, where A_t is absorbance after time '*t*' and A_o is absorbance of dye solution before degradation. (Fig. 7) shows the photocatalytic activity of pure TiO_2 and Ni^{2+}-TiO_2 samples under UV light (A), visible light (B) and direct sunlight (C). It is observed that while the pure TiO_2 sample is more efficient than the nickel doped samples in UV light irradiation, under visible and direct sunlight, percentage degradation increases with increase in Ni^{2+} concentration. The prominent feature of the synthesized catalyst is that, it is most efficient under direct sunlight in which 1.60 wt.% Ni^{2+}-TiO_2 sample degrades 90.53 % of malachite green dye in 180 min. All the samples in UV, visible and direct sunlight show a significant effect within first 60 mins, after which the rate of degradation shows slowly rise. Hence, the synthesized Ni^{2+}-TiO_2 (1.60 wt.%) photocatalyst can be efficiently used under direct natural sunlight in dye effluent treatment plants as an energy effective treatment.

Conclusions

In the present work, visible light active Ni^{2+}-TiO_2 photocatalyst was prepared by stainless steel autoclave hydrothermal method using TTIP precursor. Using this method we achieved 1.60 wt.% doping of Ni^{2+} in the pure phase anatase TiO_2. Doping of the Ni^{2+} ion decreases the particle size, which increases the surface area and also the band gap energy, yielding a highly active visible light photocatalyst. The photocatalyst Ni^{2+}-TiO_2 (1.60 wt%) showed excellent photocatalytic activity in the visible and direct sunlight. More than 90% degradation has been achieved in 180 min using this photocatalyst under sunlight. Hence the synthesied Ni^{2+}-TiO_2 (1.60 wt.%) photocatalyst can be efficiently used under direct sunlight in dye effluent treatment plants as a more energy effective treatement due to natural sunlight.

Acknowledgement

Authors are thankful to UGC-DAE Consortium for Scientific Research, Indore, India, for the TEM, XPS and Raman characterization of the samples. Authors are also thankful to Department of Science and Technology, New Delhi, India, for sanctioning grant under DST-FIST program (No/SR/FST/College-151/2013(C)) to Jaysingpur College, Jaysingpur. SS is thankful to University Grants Commission, New Delhi, India, for grants under Major Research Project [File No: 43-219/2014 (SR) Dt. 18.08.2015].

References

1 Wojtyla S & Baran T, *J Euro Bull*, 4-6 (2015) 260.
2 Velusamy P & Lakshmi G, *Indian J Chem*, 56A (2017) 43.
3 Thirumalai K, Shanthi M & Swaminathan M, *Indian J Chem*, 56A (2017) 50.
4 Song Z, Sun X & Qiu J, *Indian J Chem*, 53A (2014) 1332.
5 Rajamanickam D & Shanthi M, *Indian J Chem*, 54A (2015) 613.
6 Quinones D, Rey A, Alvarez P , Beltran F & Puma G, *J Appl Catal B: Environ*, (2014) 1
7 Chen Y, Cao X, Lin B & Gao B, *J Appl Surf Sci*, 264 (2013) 845.
8 Lai L-L, Wen W & Wu J-M, *RSC Adv*, 30 (2013) 1.
9 Kulish M, Struzhko V, Bryksa V, Murashko A & Ilin V, *J Semicond Phys Quant Electron Optoelectron*, 14 (2011) 21.
10 Wanga M, Lin H & Yang T, *J Alloys Compd*, 473 (2009) 394.
11 Kamble R, Sabale S, Chikode P, Puri V & Mahajan S, *Mater Res Express*, (2016) 3.
12 Lopez R, Gomez R & Llanos M, *Catal Today*, 148 (2009) 103.
13 Begum N, Ahmed H & Gunashekar K, *J, Bull Mater Sci*, 31 (2008) 747.
14 Subramanian M, Vijayalakshmi S, Venkataraj S & Jayavel R, *Thin Solid Films*, 516 (2008) 3776.
15 Li L, Liu C-Y & Liu Y, *Mater Chem Phys*, 113 (2009) 551.
16 Raza W, Haque H & Muneer M, *Arabian J Chem*, (2015) 1.
17 Casados-Solis D, Alarrcon-Escobar L, Fernandez M & Valencia F, *J Fuel*, 110 (2013) 17.
18 Pang Y & Abdullah A, *Appl Catal B: Environ*, 129 (2013) 473.
19 Jadhav V, Dhabbe R, Sabale S, Nikam G, Tamhankar B, *Univers J Environ Res Technol*, 3 (2013) 667.
20 Cullity B D, *Elements of X-Ray Diffraction*, Chap. 14, (Addison-Wesly Publishing Co. Inc) 1976.
21 Tripathi A, Mathpal M, Kumar P, Agrahari V, Singh M, Mishra S, Ahmad M & Agarwal A, *Adv Mater Lett*, 6 (2015) 201.
22 Choudhury B & Choudhury A, *Mater Sci Eng B*, 178 (2013) 794.
23 Lin Y-J, Chang Y-H, Yang W-D & Tsai B-S, *J Non-Crystall Solids*, 352 (2006) 789.
24 Bandgar A, Sabale S & Pawar S, *J Ceramic Int*, 33 (2012) 1905.
25 Uboncholakate K, Sikong L, Tontai T & Saito F, *J Adv Mater Res*, 150-151 (2010) 1726.
26 Yadav H, Otari S, Bohara R, Mali S, Pawar S & Delekar S, *J Photochem Photobiol Chem A*, 294 (2014) 130.
27 Cong Ye, Zhang J, Chen F, Anpo M & He D, *J Phys Chem C*, 111 (2007) 10618.
28 Choudhury B & Choudhury A, *J Mater Chem Phys*, 132 (2012) 1112.

29 Xu C, Zhang P & Yan L, *J Raman Spectroscopy*, 32 (10) (2001) 862.
30 Wagner C, Riggs W, Davis L, Moulder J & Muilenberg G, *Handbook of X-ray Photoelectron Spectroscopy*, (Perkin-Elmer Corp, Physical Electronics Division, USA) 1979.
31 Fan B, Chen Z, Liu Q, Zhang Z & Fang X, *J Appl Surf Sci*, 370 (2016) 252.
32 Tang H, Berger H, Schmid P, Levy F & Burri G, *Solid State Commum*, 87 (1993) 847.
33 Sabale S, Bandgar A, Wang H, Gurav K, Kim J & Pawar S, *Met Mater Inter*, 19 (2013) 483.